Domain Growth, Pattern Formation, and Morphology Transitions in Langmuir Monolayers. A New Growth Instability

Andrea Gutierrez-Campos, Grisell Diaz-Leines, and Rolando Castillo*

Instituto de Física, Universidad Nacional Autónoma de Mexico, P.O. Box 20-264, Mexico, D. F. 01000

Received: October 29, 2009; Revised Manuscript Received: January 22, 2010

The aims of this study are the following two: (1) To show that in Langmuir monolayers (LM) at low supersaturation, domains grow forming fractal structures without an apparent orientational order trough tip splitting dynamics, where doublons are the building blocks producing domains with a seaweed shape. When supersaturation is larger, there is a morphology transition from tip splitting to side branching. Here, structures grow with a pronounced orientational order forming dendrites, which are also fractal. We observed this behavior in different Langmuir monolayers formed by nervonic acid, dioctadecylamine, ethyl stearate, and ethyl palmitate, using Brewster angle microscopy. (2) To present experimental evidence showing an important Marangoni flow during domain growth, where the hydrodynamic transport of amphipiles overwhelms diffusion. We were able to show that the equation that governs the pattern formation in LM is a Laplacian equation in the chemical potential with the appropriate boundary conditions. However, the underlying physics involved in Langmuir monolayers is different from the underlying physics in the Mullins−Sekerka instability; diffusional processes are not involved. We found a new kind of instability that leads to pattern formation, where Marangoni flow is the key factor. We also found that the equations governing pattern formation in LM can be reduced to those used in the theory of morphology diagrams for two-dimensional diffusional growth. Our experiments agree with this diagram.

1. Introduction

During domain growth, a stable phase, usually solid, propagates into a metastable one, usually liquid. During this propagation, the interface between both phases moves as the metastable phase is transformed into the more stable one. The interface becomes unstable and forms patterns because of the competition between a temperature gradient (or chemical potential gradient) that destabilizes the interface on one hand and surface tension that stabilizes the interface on the other.[1,2] One factor increases the interface to allow heat release (or chemical migration) to grow and the other avoids the energetically expense interface. The further the system is out of equilibrium, the faster the metastable phase will turn into the stabler phase and, consequently, the faster the interface will propagate. The competition between effects that stabilize and destabilize the system gives rise to characteristic length scales of growing domains and determines, together with the stable phase anisotropy, the overall shape and symmetry of domain patterns.[1] Balance between competing effects varies as growth conditions change. The observed patterns may be grouped into a small number of typical patterns or morphologies each representing a different dominant effect. Tip-splitting growth gives rise to dense branched morphologies called seaweeds and dendritic growth, which is characterized by a needle with side branches, produces dendrites. Each morphology is observed over a range of growth conditions, bringing to mind the idea of a morphology diagram and the existence of a morphology selection principle. This one would select a particular morphology and consequently, the corresponding transitions, as we vary the growth conditions. In equilibrium, the phase that minimizes the free energy is selected and observed. The existence of an equivalent principle for out-of-equilibrium systems are one of the longest pursued and yet unsolved questions in the study of pattern formation.

Pattern formation in three-dimension (3D) has a long history.[2] First just undercooling was considered, predicting the existence of a continuous family of steady-state solutions all with parabolic shape, where the product of the tip radius and the growth velocity for each parabola was a constant, suggesting that dendrites with different tip curvatures and corresponding tip velocities could coexist at a specified undercooling. However, it was experimentally demonstrated that under controlled conditions for a given undercooling the same dendrite is reproducible, implying a selection problem.[3] To solve the selection problem, surface tension was included. Although it seemed as if the selection problem had been solved, this was not so; different substances that, accordingly to predictions, would produce dendrites, by no means did it. In addition, decoration of a needle crystal with side branches, that is, a dendrite, did not seem to influence the selected velocity dramatically, so the selection problem for the needle crystal included the one for dendrites. The selection problem for growing needle crystals was solved through the microsolvability theory with the conclusion that surface tension and surface kinetics, despite their small size, turned out to be singular perturbations to the problem that totally change the character of interfacial dynamics.[4,5] When surface tension and surface kinetics are isotropic, dendritic growth does not occur, but rather fingers with tip-splitting dynamics are observed. Anisotropy in the interfacial dynamics of the stable phase is required to produce dendritic growth.[4] A theory of pattern formation for diffusional growth was developed by Müller-Krumbhaar and co-workers, which were able to develop a morphology diagram,[6−11] where the building block of the dendritic structure is a dendrite with parabolic tip, and the basic element of the

* To whom correspondence should be addressed. E-mail: rolandoc@fisica.unam.mx. Phone: (52) 55 56225094. Fax: (52) 55 56161535.

10.1021/jp910344h
Published on Web 03/26/2010

seaweed structure is a doublon;[10,11] this is a local structure consisting of two broken-symmetry fingers that are mirror image of each other and separated by a narrow groove of liquid of constant width. The control parameters in the morphology diagram are the anisotropy of the capillary length and the undercooling. The predicted structures are classified according to whether they are compact or fractal, and whether they possess orientational order or not. Different morphologies after changing the control parameters have been observed, as in the directional solidification of succinonitrile alloys that show different morphologies depending on the plane direction where they grow,[12] or in the observation of morphology transitions from dendrites to seaweeds in xenon 3D crystals.[13,14]

Studies of patterns formed by growing domains in Langmuir monolayers (LMs) are not common. Pattern formation in phospholipids has been explained in terms of a 2D diffusion model with impurities, since a dye was used to observe the monolayer with polarized fluorescence microscopy.[15] Dendritic growth in the chiral amphiphile D-myristoyl alanine has been studied in the context of the microsolvability theory.[16] Also, a variety of nonequilibrium growth structures have been reported for monolayers of fatty acid ethyl esters (palmitate and stearate),[17] 1-monopalmitoyl-*rac*-glycerol,[18] cis-unsaturated fatty acids,[19] dioctadecyamine,[20] and mixtures of phosphatidylcholine and ceramide.[21] There are also studies of chiral effects on the shape of domains for different enantiomeric and racemic mixtures of phospholipids[22−25] and N-acyl amino acids.[26] In LMs made of a single component, the problem of nonequilibrium growth morphologies is subtler than in 3D solids. In the latter case, the heat released during the phase transition has to be diffused far away from the interface before the front can advance further. This mechanism can be ruled out in LMs because the monolayer rests on a large body of water (subphase) that acts as an isothermal reservoir, absorbing all the latent heat released during the phase transition. So, it is not clear why patterns are formed in LMs. Growing instabilities are usually observed along a fluid/nonfluid phase transition (LE/LC, LE/S), where the involved phases have a large difference in area density (∼50%). Amphiphiles usually have some kind of hindrance (2 or more tails, a chiral center, bent tails due to double bonds, and so forth). Supersaturation induces domain growth, which depending on the experimental conditions forms either seaweed or dendritic morphologies. The interest of studying how patterns are formed in monolayer domains relies on questions that are not satisfactory solved, for instance, if heat is not playing a role, why does a complex morphology evolve in uniform environments? Why do we not simply observe growing 2D circular domains? How are length scales selected as tip-radius, width and spacing of the side-braches? Why does the morphology of a growing domain change from tip splitting to side branching? To answer some of these questions, our group has recently presented a study of how domain patterns are formed in LMs and how their morphology evolves.[27,28] There, we found morphology transitions from tip splitting to side branching. Also, we observed the formation of doublons during domain growth, including the onset of the instability in round domains when an abrupt lateral pressure jump is made on the monolayer. It was found that as domain growth starts, the shape becomes unstable. At low supersaturation, some unstable modes grow faster and structures evolve through tip-splitting dynamics. At high supersaturation levels, there is a morphological transition where domains grow with needle tips, which show, as growth proceeds, side branching. Nevertheless, we did not address the issue of classification of the growth structures that could be compact or fractal patterns. By compact growth we mean growth at constant density, irrespective of the value of this density, while in a fractal pattern the density varies with length scale. In that study,[27,28] a model was proposed to understand this kind of nonequilibrium growth patterns. At the steady state, the growth behavior is supposedly determined by a density profile around domains due to the large density difference between the metastable phase with respect to the stable one. This density profile drives amphiphile molecules toward the LE/LC line boundary by diffusion, suggesting a Laplace's equation in chemical potential with specific boundary conditions, which are equivalent to those used in the theory of morphology diagrams for two-dimensional diffusional growth developed by Müller-Krumbhaar and collaborators,[6−11] where morphological structures and morphological transitions can be obtained. This description is different from the one presented by R. Bruinsma et al.,[29] not experimentally tested yet, where it was proposed that a hydrodynamic mechanism based on the Marangoni flow describes the growth instabilities of domains in monolayers, using a 2D equation equivalent to the Stokes equation. Two regimes predicting different pattern evolution were theoretically analyzed, when the steady growth is dominated by the bulk viscous term or by the surface viscous term. In this description, the issue of morphological structures and morphological transitions is not addressed.

The main topics to be presented in this paper are the following: (a) Experimental results showing how domains grow at low supersaturation forming fractal structures without an apparent orientational order trough tip splitting dynamics with doublons as the building blocks producing domains with a fractal seaweed shape. When supersaturation is larger, there is a morphology transition from tip splitting to side branching, that is, structures with a pronounced orientational order (dendrites) are formed, which are also fractal. This behavior can be observed in different LMs at the air/water interface, using Brewster angle microscopy (BAM). We will concentrate on experimental results for the nervonic acid (NA) monolayer, however, we also include results from other monolayers such as dioctadecylamine (DODA), ethyl stearate (ES), and ethyl palmitate (EP). (b) Experimental results revealing Marangoni flow close to the growing domains, obtained using a new technique that allows us to measure flows in the vicinity of growing domains, using hydrophobized silica microspheres as tracers. This experimental evidence supports that patterns are formed by a hydrodynamic mechanism where Marangoni flow is important. In steady state, growth is apparently dominated by the bulk subphase viscous term although the surface viscous term cannot be neglected. (c) A model where a Laplacian equation in the chemical potential can be recovered from the hydrodynamic model with Marangoni flow, including the necessary boundary conditions, to explain the morphology structures and the morphology transitions, as previously reported.[27,28] Our experiments agree with the kinetic morphology diagram.[6−11] However, the underlying physics involved in LM is different from the underlying physics in the Mullins−Sekerka instability; diffusional processes are not involved. This is a new kind of instability that leads to pattern formation, where Marangoni flow is the key factor.

2. Models to Explain Pattern Formation in Langmuir Monolayers

Two models have been presented to explain the pattern formation in LMs. In the first one,[29] the growth instability is due to a hydrodynamic mechanism where concentration gradients produced by supersaturation generate a hydrodynamic flow

through the Marangoni effect, and only inside a very narrow strip of molecular size outside the LE/LC boundary transport takes place by diffusion. Here, local fluid velocities at the air/water surface produce a modulated LE/LC boundary, and flow lines are focused toward the tips of the boundary. As a consequence, excess of surfactant is transported to the tips of the LE/LC boundary, which increases the amplitude of the modulation. On the other hand, the second model[27,28] pays attention on the large density difference (~50%) of the involved phases in domain growth. Here, the basic assumption is that domain growth will necessarily give rise to a density profile of the order of several micrometers in length in the domain neighborhood. Diffusion is the key factor driving amphiphile molecules toward the LE/LC line boundary; subduction flow does not play an important role. In addition, this model could be related to the theory of dynamic phase transitions,[6−11] to understand the morphological structures and morphological transitions.

To focus on the main differences between both models that will be confronted in this paper, let us present here the main variables used to describe growth in a LM. Here, we will represent by LE the liquid expanded phase, and by LC any condensed phase. We denote by μ the chemical potential of amphiphile molecules, which is the same for both phases when the interface is flat or when the interface curvature is negligible; let us denote it by μ_o. ρ_l and ρ_s are the amphiphile densities for LE and LC phases, respectively. If we impose a small, but abrupt, decrease in the total area occupied by the LM, as in the experiments to be described below, a transient increase in surface pressure ensues. Far from the LE/LC line boundary, both the amphiphile density and chemical potential in the LE phase increase by amounts $\delta\rho$ and $\delta\mu$, respectively. The chemical potential μ_0 and the density ρ_s in the LC phase change only by a negligible amount. For sufficiently low levels of supersaturation, that is, for sufficiently small values of $\delta\rho$ and $\delta\mu$, we can employ the condition of local thermodynamic equilibrium. Under these conditions, we reach a stationary state, where the chemical potential is a continuous function of position, and it must be equal on both sides of the LE/LC flat line boundary. Away from this LE/LC line boundary, μ increases monotonically until it reaches a value $\mu_\infty = \mu_0 + \delta\mu$ at the monolayer boundary. Density increases also monotonically from the line boundary until it reaches the asymptotic value $\rho_\infty = \rho_0 + \delta\rho$. Now, consider that the monolayer is mainly in a LE phase coexisting with a few LC domains at temperature, T, in a stationary state, where the boundary of the LC domains has a local curvature κ. Therefore, we need to bring into play the Gibbs−Thomson equation at the line interface

$$\mu(\text{interface}) - \mu_0(T) = -\frac{\tau}{\Delta\rho}\kappa \tag{1}$$

where $\Delta\rho$ is the equilibrium density difference between LE and LC phases at the temperature T, and τ is the line tension. Inevitably, there is another boundary condition related to the mass conservation at the LE/LC boundary

$$v_n = \frac{M}{\Delta\rho}[\beta(\nabla_\perp\mu)_s - (\nabla_\perp\mu)_l]\cdot n \tag{2}$$

where v_n is the normal velocity of the line interface, and $\beta = M'/M$ is the ratio of LC to LE mobilities, M' and M, respectively; the diffusion coefficient is $D = M(\partial\mu/\partial\rho)$. We will also consider that the subphase has an infinite depth in the y-direction, and it is also infinite as the monolayer in the perpendicular directions, $\perp$, that is, the plane where the monolayer rests. The subphase flow velocity $v(x,y,z)$ obeys the usual 3D Stokes equation for incompressible liquids

$$\nabla\cdot v(x,y,z) = 0 \tag{3}$$

In all our theoretical description, we will use a reference frame attached to the moving boundary. Under steady-state conditions the concentration flow profiles are time independent in this frame.

In the hydrodynamic model, as a consequence of Marangoni effect, a hydrodynamic flow is predicted. Here, the basic equations in the steady-state for describing the monolayer are given by the 2D equivalent Stokes equation[29,30]

$$\eta_s\nabla_\perp^2 v(x, y=0, z) = \left|\frac{d\gamma}{d\rho}\right|\nabla_\perp\rho_l(x,z) - \eta\partial_y v(x, y=0, z) \tag{4}$$

and by the mass conservation equation

$$\nabla_\perp\cdot J(x, y=0, z) = 0 \tag{5}$$

where

$$J(x, y=0, z) = \rho_l(x, y=0, z)v(x, y=0, z) - D\nabla_\perp\rho_l(x, y=0, z) \tag{6}$$

In these equations $\nabla_\perp$ is the operator that applies only to the in-plane coordinates, γ is the surface tension, η_s and η are the monolayer and the subphase viscosities, respectively. To compare the relative importance of surface and the viscous terms in eq 4 is critical, and it is necessary to note that the ratio of the surface to the subphase bulk viscous terms is of the order $q\zeta$;[29] $\zeta = \eta_s/\eta$ and $q = 2\pi/l$, where l is a relevant periodicity size of LC domains in a supersaturated LE phase following a mechanical compression. Therefore, there are two regimes easily defined that were studied by Bruinsma et al.[29] Surfaces viscous losses are dominant when $q\zeta \gg 1$. This limit can lead to the diffusional model.[8] On the contrary, bulk viscous terms dominate when $q\zeta \ll 1$. Transport and instability mechanisms are mathematically different in both regimes. In this paper, we will try to determine which regime is followed during domain growth.

In the diffusional model at the steady state, the growth behavior is determined by a density profile around domains, which generates a diffusion zone, due to the huge density difference between LC and LE phases. The density profile is supposed to be of the order of several micrometers in length around the domain neighborhood, and it is the result of a mass balance that drives amphiphile molecules toward the LE/LC line. Thus, the monolayer growth is governed by the equation

$$\nabla_\perp^2\mu = 0 \tag{7}$$

Equation 7 has to be solved with the two boundary conditions (1) and (2). They are similar to the equations used by Müller-Krumbhaar[6−11] and collaborators to analytically build a

kinetic morphology phase diagram, where they include in the Gibbs−Thomson equation a supersaturation parameter Δ, and a capillary length with an anisotropy parameter, ε, that is, $d = d_0 (1 - \varepsilon \cos n\theta)$. Here, d_0 is the so-called capillary length defined by $d_0 = \tau [(\Delta\rho)^2(\partial\mu/\partial\rho)]^{-1}$. The diagram predicted by those authors has regions of different morphological structures and lines indicating transitions between them, defined by the control parameters Δ and ε. They could discriminate between compact and fractal structures, as well as between structures with orientational order, like dendrites, and structures without apparent orientational order, as seaweeds. In the same way in LMs, the transitions between morphological structures must be also related to changes in the control parameters during domain growth (supersaturation level and line tension anisotropy). In addition, in the diffusional model, it was also possible to obtain a dispersion relation that could explain which modes of growth preserve the circular shape and which ones become unstable.[26,27]

Physics behind the hydrodynamic and the diffusional models are different. Therefore, one issue to be addressed in this paper is to find out if there is a density profile where amphiphiles move mainly driven by diffusion or if they move mainly due to a hydrodynamic flow occurring in the subphase and in LE, induced by the concentration or a chemical potential difference, that is, Marangoni flow. The key would be to discern if growth is dominated by viscous dissipation in the subphase or by viscous dissipation at the monolayer. Our findings leaded us to propose a better model to understand pattern formation in LMs in the last section.

3. Experimental Section

3.1. Amphiphiles. Dioctadecylamine (DODA), 2C18NH (≥99%), was purchased from Fluka Chemie (Switzerland). Nervonic acid (NA) (≥99%), ethyl stearate (ES) (99%), and ethyl palmitate (EP) (≥99%) were obtained from Sigma Aldrich Inc. (MO, U.S.A.). All of them were used without further purification.

3.2. Monolayers. Measurements of the pressure−area isotherms, $\Pi(A,T) = \gamma_0(T) - \gamma(A,T)$, were performed spreading the amphiphiles in solution onto a subphase made of ultrapure water (Nanopure-UV, 18.3 MΩ) in a Langmuir trough. After a waiting time for allowing evaporation of the solvent coming from the spreading solution, the monolayer was slowly compressed. T is the temperature, A is the area/molecule, and γ and γ_0 are the surface tensions of the monolayer and of the uncovered subphase, respectively. The spreading solution was made with chloroform (Aldrich, U.S.A., HPLC) for DODA and NA monolayers and with heptane (Aldrich U.S.A., ≥99%) for EP monolayer and in all cases at a concentration of 1 mg/mL. The DODA monolayer subphase was modified with H_2SO_4 (Merck, Mexico) to reach pH 3. The other monolayers were worked at pH 5.7−5.8. On many occasions, we modified the subphase viscosity by adding glycerol (≥99%) from Sigma Aldrich Inc. (MO, U.S.A.). When the subphase glycerol concentration was up to 10 vol %, the dynamics of domain growth was sensibly slowed without an appreciable change in the isotherms or in the phase transition texture.

3.3. Troughs. Two NIMA troughs (601 BAM and 601 M, Nima Technology Ltd., England) were used. The trough used to observe the domain growth in DODA and hydrodynamic fluxes in EP is a rectangular one with a working area starting at 490 cm^2, and it rests on a vibration isolation system (model 2S, Halcyonics GmbH, Germany). The trough used for NA is also a rectangular one but smaller, with a working area starting at 84 cm^2 and it rests on an optical table to avoid vibrations (model 13811, Oriel Corporation, U.S.A.). Both troughs are made of PTFE and were put inside of a 1 m^3 plastic box to avoid undesired air convection. The temperature difference between the surroundings defined by the air inside the box and the trough was at most 1 °C. Additionally, a C-shaped piece of Teflon with stainless steel inside was used with the NA monolayer to slow the global monolayer movement. In both cases, a Wilhelmy plate was used to measure Π, and temperature was kept constant with the aid of a water circulator bath (Cole-Parmer 1268-14 and 12101-00, U.S.A.). All experiments were carried out in a clean-room lab.

3.4. BAM. The growth of domains was observed with an Elli2000 imaging ellipsometer (Nanofilm Technologie GmbH, Germany) in the BAM mode (spatial resolution of ∼2 and ∼1 μm using the 10× and 20× objectives, respectively). When the monolayer moved slowly, this instrument allowed us to get observations with the whole field of view in focus, due to its movable objective lens. A BAM1 plus instrument (Nanofilm Technologie GmbH, Germany) was also used to obtain NA images with a spatial resolution of ∼4 μm. This instrument allowed us to follow some growing domains due to its capability of *XY* motion.

3.5. Microspheres. Silica beads (with silanol (SiOH) surface groups) were purchased from Bangs Laboratories, Inc. (U.S.A.) with a mean diameter of 2.47 μm (10 wt %, solids). The density of the microspheres is *2.0 g/cm³*, so they do not float on the subphase. However, if beads are treated with 8−10 times centrifugation−sonication cycles in a chloroform-ethanol mixture, they end up hydrophobized, allowing them to float on the air/water interface. We used another procedure to hydrophobize the microspheres through functionalizing them with octadecyltrichlorosilane (OTS) by using a condensation reaction between the OTS and the silanol surface groups of microspheres in ethanol. Both methods produced floating beads with similar tracer properties. A 1 wt % bead suspension in a 1:1 chloroform−ethanol mixture was prepared. Eighty microliters of this suspension were mixed with 5 mL of the monolayer spreading solution. This new suspension is the actual spreading solution to deposit amphiphiles and microspheres at the same time on the air/water interface.

3.6. Contact Angle Measurements. To determine the hydrophobized particle−fluid contact angle, we used the method developed by Sickert et al[31] that consists in forming a sessile water drop on the surface of a siliconized glass cover microscope slide (Hampton Research, U.S.A.) and depositing a dilute solution of microspheres on its surface. Beads sediment by gravity toward the glass−water contact line, where they are observed with an inverted microscope through a long working distance objective (M plan Apo 100× Mitutoyo, Japan).

3.7. Surface Tension and Density Measurements. The surface tension of a water/glycerol mixture was measured by the falling drop method counting drops when the fluid flows between two arbitrary marks on a capillary. The density was measured using a calibrated picnometer (10.149 cm^3 at 20.2 °C, Brand, Germany).

3.8. Fractal Dimension Measurements. Brightness and contrast of BAM images of NA, DODA, and EP monolayers were adjusted using software (ImageJ 1.42 g, Wayne Rasband, National Institutes of Health, U.S.A., and/or Adobe Photoshop 8.0.1, Adobe Systems Inc., U.S.A.). Fractal dimension was measured by using the box counting method implemented in the software FRACLAC 2.5 Release 1d plugin for ImageJ (developed by A. Karperien, Charles Sturt University, Australia).

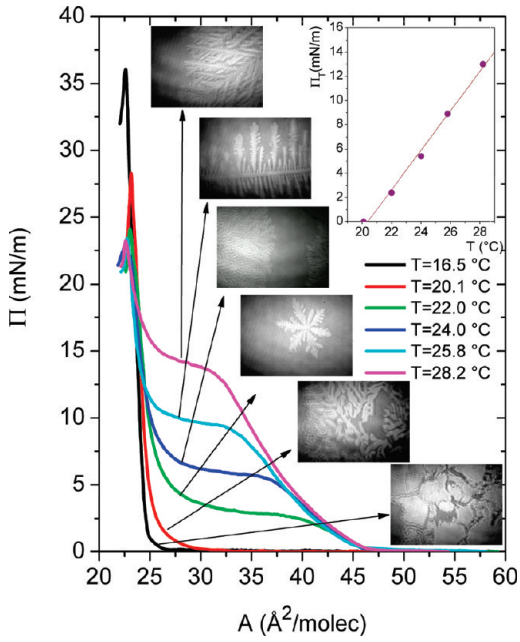

Figure 1. Π-A isotherms for NA monolayer at different temperatures (pH = 5.7−5.8) and BAM images at the LE/LC coexistence. Inset: Temperature dependence of the phase transition equilibrium pressure.

4. Results and Discussion

4.1. Compression Isotherms and their BAM Observation. As far as we know, there are two previous reports where compression isotherms for NA monolayer were presented (pH = 3).[19,32] However, they differ in the coexistence plateau lateral pressure. For that reason, we developed our own compression isotherms, which were observed with BAM before starting the pattern formation study for this monolayer. In Figure 1, we present the Π-A isotherms for the NA monolayer at different temperatures (pH = 5.7−5.8). At the same time, during the compression process, monolayers were surveyed with BAM. At negligible pressures, we found gas phase (G) coexisting with a liquid expanded phase (LE) when temperature is above $T \sim 20.5$ °C. Below this temperature, G is coexisting with a more solid-like phase that we named as liquid condensed phase (LC). As lateral pressure increases during compression, there is a first order transition between LE and LC phases for temperatures above $T \sim 20.5$ °C. Along a wide coexistence plateau, beautiful patterns to be described below are formed by the growing domains of LC phase. The LC phase is quite incompressible; a typical compressibility, $\kappa = -1/A\ (\partial A/\partial \Pi)_T$, value is 4.6×10^{-3} m/mN (22 °C). As previously reported,[33] LC phase forms a centered rectangular lattice with alkyl chains tilted toward their NN direction. After a long relaxation time, LC domains show two planes of symmetry in agreement with the reported lattice. The effect of lateral pressure on tilt (∼25 − 31 °C) and on in-plane molecule area (∼23.2 Å²/molec) has been reported as small.[32] Below $T \sim 20.5$ °C, the LE/LC coexistence disappears and we just found the G/LC coexistence. Collapse is found between 27−35 mN/m depending on temperature; the lower the temperature, the higher collapse pressure. Our compression isotherms are closer to those reported by Iimura et al.[19] The inset of Figure 1 presents the temperature dependence of the LE/LC phase transition equilibrium pressure Π_e. In the short temperature range under study, Π_e is a linear function of temperature ($\Pi_e = 1.63T - 33.14$ mN/m). Our $d\Pi_e/dT = 1.63$ mN/m K^{-1} value is close to the values obtained for other two-tail amphiphile monolayers as DMPC (2.35 mN/m K^{-1}),[33] DMPA (1.05 mN/m K^{-1}),[33] DODA (1.26 mN/m K^{-1}),[20] and r-DPPC (1.42 mN/m K^{-1}).[34] Using the Classius−Clayperon equation ($l = \Delta A T\ d\Pi_e/dT$, ΔA corresponds to the molecular area difference between LC and LE phases at the onset of the transition) the latent heat was evaluated as $l = 47.90$ kJ/mol at 22 °C. This value is larger than one previously reported for NA (∼18.5 kJ/mol);[32] the difference can be attributed to the difference between our compression isotherms and those presented in that work. Our l is of the same order of DPPC monolayer[34] (114 kJ/mol) at 20 °C and of DODA monolayer (89.86 kJ/mol).[20] pH modifies to some extent isotherms. In particular *pH* slightly modifies the position of the LE/LC coexistence. The larger *pH* presents the larger Π_e. However, BAM images do not show any significant difference among domains at those pH values. Collapse pressures are ∼45 mN/m at pH = 7 and ∼ 24 mN/m at pH 3−5.7 ($T = 22.0$ °C).

4.2. Pressure Jumps. Morphology of domain growth of LC phase for the NA monolayer was observed performing several experiments using pressure jumps. First, the monolayer was compressed up to the phase transition, i.e., when LE and LC are in coexistence (at the kink point in the Π-A isotherm at the onset of the phase transition). After some minutes to allow monolayer relaxation (∼3−5 min), a pressure jump was made by a sudden compression of the monolayer to supersaturate the system. This sudden supersaturation jump is equivalent to an undercooling jump in classical solidification. The pressure reached after the jump was maintained constant using the servomechanism of the Langmuir trough.

Figure 2a shows typical BAM images of the NA monolayer ($T = 21.9$ °C) after a pressure jump of $\Delta\Pi = 1$ mN/m, where the monolayer reaches an actual pressure of $\Pi = 3.5$ mN/m. Particularly, in this example we present a series of four successive images, where we can observe how a couple of growing domains evolve as time elapses (time step ∼10 s). Domains grow forming seaweedlike structures, caused by the typical tip-splitting dynamics. This is particularly clear at the tip of the main stems of the seaweedlike structures. At the end of many seaweed arms, doublons are easily observed. However, in spite that local growing conditions along the trough are surely not exactly the same, we observed only seaweeds along the monolayer. When the pressure jump above equilibrium is of $\Delta\Pi = 2$ mN/m to reach a lateral pressure of $\Pi = 5$ mN/m, we observe essentially the same kind of growing as before, although tip-splitting dynamics forming seaweeds is more clear. This is shown in a typical sequence of images presented in Figure 2b developed at $T = 21.8$ °C, where the growth of one domain is followed. Figure 3a presents a sequence of images when the pressure jump is $\Delta\Pi = 3$ mN/m (final pressure reached $\Pi =$ 4 mN/m, $T = 21.8$ °C). Here, although domains are growing through tip-splitting dynamics, it is clear that something has changed. The arms of domains are not as slim as before; they form like triangular-shaped stems. At this supersaturation level, the monolayer seems to be close to a transition zone where morphology will change. This occurs when the pressure jump reaches values of $\Delta\Pi = 4$ mN/m. In Figure 3b, we present several images of the monolayer when the supersaturation is larger than that in the preceding examples due to a big pressure jump of $\Delta\Pi = 4$ mN/m, lateral pressure reaches an actual value of $\Pi = 5$ mN/m, $T = 21.9$ °C. Here, dendrites are the most common growing structures. The arms of the growing domains are mainly formed by needles with side branches. It is common to find some arm in a domain that is growing with tip splitting, particularly when this arm is to close to other growing domains. Finally, a global observation of Figures 2 and 3, where the

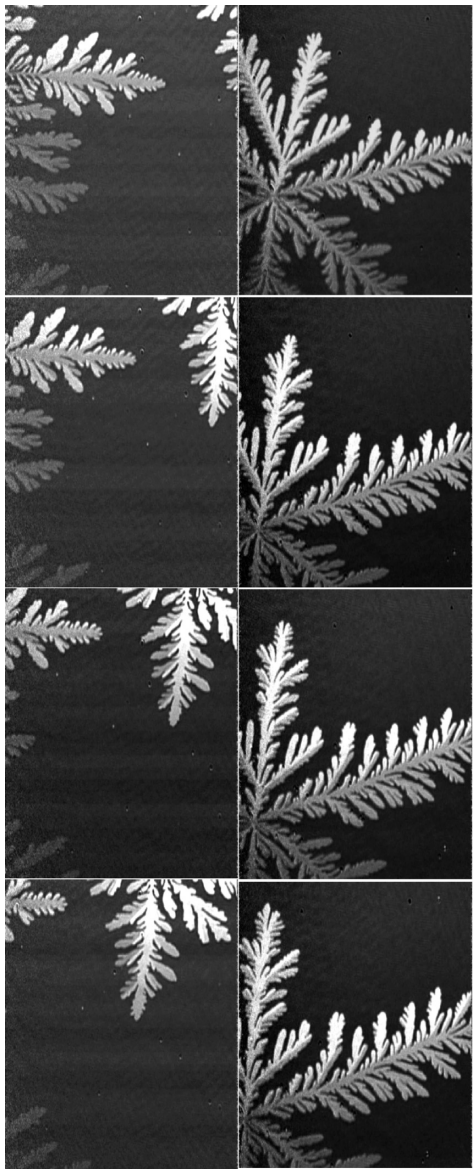

Figure 2. BAM images of NA monolayer. (Left vertical strip) After a pressure jump of $\Delta\Pi = 1$ mN/m that reaches a final pressure of $\Pi = 3.5$ mN/m (elapsed time after the pressure jump ~70, 80, 90, and 100 s, top to bottom; $T = 21.9$ °C). (Right vertical strip) After a pressure jump of $\Delta\Pi = 2$ mN/m that reaches a final pressure of $\Pi = 5$ mN/m (elapsed time after the pressure jump ~180, 200, 210, and 230 s, top to bottom; $T = 21.8$ °C). The horizontal full width is 460 μm for each individual image.

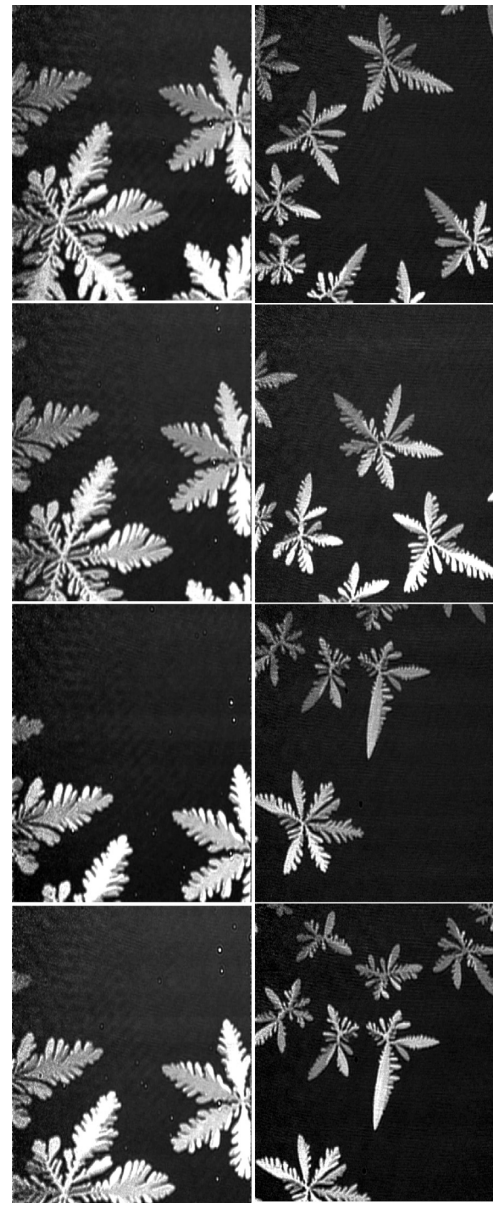

Figure 3. BAM images of NA monolayer. (Left vertical strip) After a pressure jump of $\Delta\Pi = 3$ mN/m that reaches a final pressure of $\Pi = 4$ mN/m (elapsed time after the pressure jump ~200, 210, 220, and 230 s, top to bottom; $T = 21.81$ °C). (Right vertical strip) After a pressure jump of $\Delta\Pi$=4 mN/m that reach a final pressure of $\Pi = 5$ mN/m (elapsed time after the pressure jump ~150, 160, 200, and 210 s, top to bottom; $T = 21.9$ °C). The horizontal full width is 460 μm for each individual image.

essential difference among them is just the magnitude of the pressure jumps that leads to different supersaturation levels (temperature is almost the same), makes clear that at low supersaturation levels tip splitting growth is preferred; seaweed structures are produced. On the contrary, at large supersaturation levels, side-branching growth is preferred and dendrites are formed.

4.3. Morphological Growth in Different Monolayers. The evolution just described where the monolayer prefers to grow at low supersaturation levels through tip-splitting dynamics forming doublons and then seaweeds, and as supersaturation increases, to grow through needles with side branching forming dendrites, turns out a natural question: Is that a general feature in Langmuir monolayers? The answer seems to be affirmative up to now. All monolayers that we have studied presented the same morphological evolution. Of course, more pattern formation studies have to be done in LMs to have a definitive answer. In Figure 4, we present images for different monolayers (DODA, EP, and ES) where domains are growing with the same morphology as in NA at low supersaturation levels. At high supersaturation levels, as in NA, these monolayers present a morphological transition and domains grow with side branching morphology (Figure 5). According to the kinetic morphological diagram found for diffusional growth,[7−9] the parameter that is driving the morphology change is line tension that seems to be isotropic at low supersaturation and apparently as supersaturation increases, it becomes anisotropic. We will come back to this issue later.

4.4. Compact and Fractal Patterns. To determine what kind of structures are present in LM when they are growing, we used the box-counting method, as described in the Experimental

Figure 4. BAM images of growing domains showing the same morphology as in NA. (Upper panel) DODA after 3 pressure jumps of $\Delta\Pi = 1$ mN/m reaching a final pressure of 9 mN/m; $T = 24.7$ °C. (Middle panel) Ethyl palmitate after 2 pressure jumps of $\Delta\Pi = 2$ mN/m reaching a final pressure of 8 mN/m; $T = 19.8$ °C. In top and middle panels, the horizontal full width is 220 μm. (Lower panel) Ethyl estearate before the morphological transition during a continuous compression at $T = 32.0$ °C. The horizontal full width is 460 μm.

Section, to measure the fractal dimension of domain boundaries on BAM images coming from growing patterns developed in different conditions of supersaturation for three monolayers, NA, DODA, and EP. To avoid artifacts, domains have to cover a large portion of the selected images. They were contrasted for avoiding generating structures below the limit of resolution of BAM images. Figure 6 presents a log(box number) − log(length) scaling plot for growing domains presenting both tip-splitting and side-branching dynamics. We cover at least an order of magnitude of the length scale. The fractal dimension, D, for NA monolayer is $D = 1.6$ for both kinds of domain growth. For DODA, monolayer is $D = 1.3$ for tip-splitting growth and $D = 1.4$ for side-branching growth. For ethyl palmitate, monolayer is $D = 1.4$ for tip-splitting growth, and for side-branching growth we did not obtain a good enough

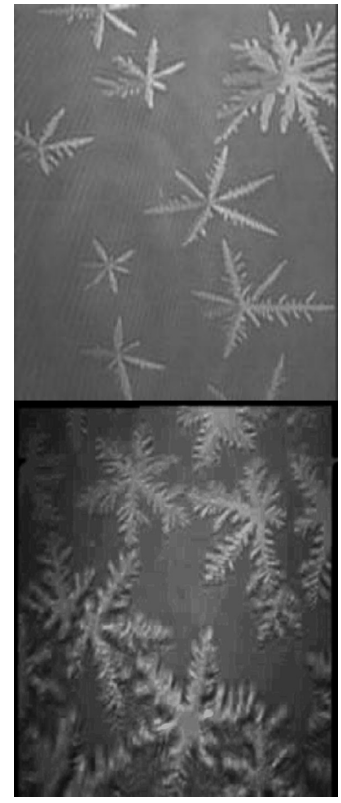

Figure 5. BAM images of growing domains showing the same morphology as in NA. (Upper panel) DODA after a pressure jump of $\Delta\Pi = 4$ mN/m reaching a final pressure of 8 mN/m; $T = 23.5$ °C. The horizontal full width is 220 μm. (Lower panel) Ethyl stearate after the morphological transition during a continuous compression at $T = 32.0$ °C. The horizontal full width is 460 μm.

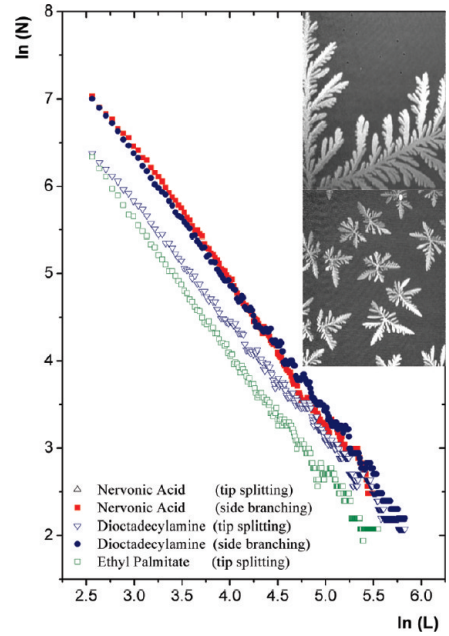

Figure 6. Log(box number) − log(length) scaling plot for growing domains presenting both tip-splitting and side-branching dynamics for different monolayers.

images to make this fractal analysis. Figure 7 presents how fractal dimension evolves during domain growth from $D = 1$ (compact domain) to $D = 1.4$ (fractal domain) as time elapses for the EP monolayer after two pressure jumps of $\Delta\Pi = 2$ mN/m, reaching a final pressure of $\Pi = 8$ mN/m; here, the box-

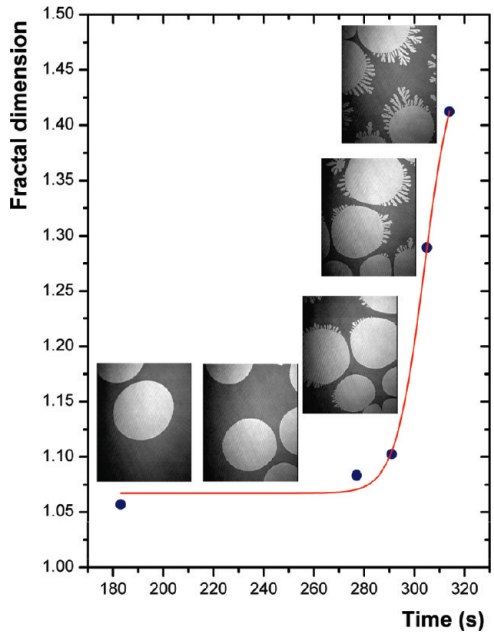

Figure 7. Fractal dimension evolution of growing domains from $D = 1$ to $D = 1.4$ as time elapses for EP monolayer after 2 pressure jumps of $\Delta\Pi = 2$ mN/m, reaching a final pressure of 8 mN/m.

counting method was also employed. It is not shown in our images, but as we reach equilibrium long time after, fractal dimension goes back again to $D = 1$ (compact domain) in this monolayer.

4.5. Experimental Measurements for $q\zeta$ Values: Diffusion Coefficients, Contact Angle, and Monolayer Viscosities. As mentioned in Section 2, to compare the relative importance of the surface and the bulk viscous terms in eq 4, it is necessary to evaluate the ratio of surface to bulk viscosity, ζ. A practical route for the rheological characterization of LMs of amphiphilic molecules spread at the air/water interface was introduced by Sickert and Rondelez,[31,35−37] who optically tracked the motion of microspherical particles placed on the interface to obtain the diffusion coefficient of microspheres, as a means to obtain the monolayer viscosity. The method used to get the diffusion coefficient is similar to that developed to follow gold nanoparticles in random motion in monolayers by fluorescent optical microscopy.[38,39] Surface viscosity can be obtained from Brownian motion of floating particles, if there is a model that takes into account the protrusion of the spheres into the subphase and the incompressibility of the viscous monolayer. A theory that incorporates these two ingredients was developed by Fischer et al.[40] and it will be used in our data analysis here.

To get the actual LE phase viscosity along the LE/LC coexistence, the experiments for tracking particle motion have been performed in the LE phase at a density corresponding to the kink that marks the onset of the phase separation. However, care was taken to be very far from domains in the case they appeared, to avoid any kind of interaction between particles and domains. Relative positions between several pairs of hydrophobized silica microspheres as a function of time, moving in Brownian motion, were obtained in each experiment. In our experiments, a BAM microscope was employed instead of an optical microscope to track the particle motion. The mean square displacement (MSD), $\langle \Delta \boldsymbol{r}^2 \rangle$, can be obtained from the relative position of a pair of microspheres as time elapses using the following equation

$$\langle \Delta \boldsymbol{r}^2(k\Delta t) \rangle = \frac{1}{(N+1)-k} \sum_{j=1}^{(N+1)-k} (\boldsymbol{r}_{j+k} - \boldsymbol{r}_j)^2 \qquad (8)$$

where $\boldsymbol{r}_{j+k}$ is the relative position of the pair of particles under observation at the $(j+k)$ step at time $(j+k)\Delta t$, $\boldsymbol{r}_j$ is the relative position at step j at time $j\Delta t$ along their relative random trajectory made of a total number of N steps; Δt is the time interval between steps ($\Delta t = 1/25$ s). The linear Stokes−Einstein relationship $\langle \Delta \boldsymbol{r}^2 \rangle = 4Dt$, is observed for relative short time intervals ($t < 1$ s) in this method.[31,35−37] For larger intervals, the behavior of the $\langle \Delta \boldsymbol{r}^2 \rangle$ is much more erratic, due to the difference in the number of data points which can be used for the averaging. The first point in that relationship is calculated using 250 relative particle positions, whereas the last one corresponds to a single event. Significant variability in the shape of the curve is observed between different microspheres in the same sample, as well as from sample to sample. Each particle pair produces two diffusion coefficients, one per each orthogonal direction. We just used trajectories for which the mean square displacements along orthogonal directions differ at most 20%, to avoid including local inhomogeneous drifts superimposed on the Brownian motion. Therefore, we averaged all the results for all the particle pairs followed in each experiment. In Figure 8, we present typical examples of MSD for microspheres along orthogonal directions for an uncovered subphase made of pure water, and for covered subphases with the LE phase of NA and with the LE phase of EP. Our results with the particle diffusion coefficients are presented in Table I for several cases. (a) For uncovered subphases made of pure water and of water and glycerin (7.3%). (b) For LE phases of NA and of EP. For the latter, we measured the MSD when the subphase was pure water and when the subphase was made of water and glycerin (7.3%). Our result for uncovered pure water, 1.22 μm^2 s^{-1}, is very close to the value obtained by Sickert et al.[31] (1.26 μm^2 s^{-1}); glycerin addition does not modify particle diffusivity noticeably. The diffusion coefficients for particles moving in the LE phases are lower than the diffusion coefficients for particles moving in the uncovered subphase, as in the case of Sickert et al.[31] For them, the ratios of particle diffusion coefficients between those moving on LE phases and those on pure water interface, at densities similar to those of interest here, was in the range of ∼0.5−0.7 for pentadecanoic acid and DPPC. This ratio is similar for NA (0.70) and EP (0.59).

Fischer et al.[40] have studied how to obtain the drag force, $F_{drag} = -\xi v$, for a microsphere that is partially immersed in an interface moving at velocity v, where ξ is the drag factor. The drag factor monotonically increases with the immersion depth of the microsphere. They found a way to calculate the drag factor using the formula $\xi = \eta R(K_T^0(\theta) + EK_T^{(1)}(\theta))$, where the $K_T^{(i)}$ are the drag coefficients that can be numerically evaluated, $E = \eta_s/\eta R$, and θ is the contact angle that is related to the depth of immersion of the particle of radius R.[31] If the drag factor for a particle immersed in a free surface is denoted by $\xi_0(\theta_0)$, where θ_0 is the contact angle between the uncovered subphase and the particle, viscosity data can be obtained by using the following expression

$$\frac{D_1}{D_0} = \frac{K_T^{(0)}(\theta_0)}{[K_T^{(0)}(\theta_1) + EK_T^{(1)}(\theta_1)]} \qquad (9)$$

Here, D_1 is the measured diffusion coefficient for immersed microspheres in a surface covered with a monolayer and D_0 is

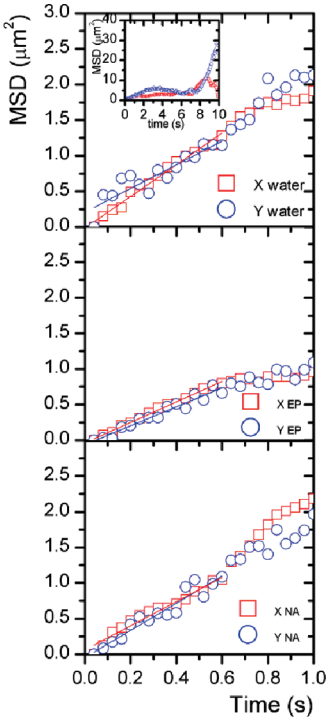

Figure 8. Examples of $<\Delta r^2>$ as a function of time for microspheres along orthogonal directions for an uncovered subphase made of pure water ($T = 22.8$ °C) upper panel, for a subphase covered with LE phase of NA ($T = 22.8$ °C) middle panel, and of EP ($T = 22.0$ °C) lower panel. Inset in upper panel: The whole relative MSD as a function of time.

TABLE I: Main Results from the Experiments of Particle Motion Tracking

	D (μm^2/s)	θ (°)	η_s (Ns/m)	$\zeta = \eta_s/\eta$ (m)
water	1.22	43.3		
water + glycerin	1.19	44.5		
NA subphase: W	0.86	40.8	1.6×10^{-9}	1.6×10^{-6}
EP subphase: W	0.72	37.2	2.7×10^{-9}	2.7×10^{-6}
EP subphase: W + glycerin	0.67	38.0	3.8×10^{-9}	3.8×10^{-6}

the same but for an uncovered interface, the θ values are experimentally measured contact angles; θ_1 is for the covered surface. The uncovered subphase contact angle was obtained using the sessile water drop described in the Experimental Section. The contact angle when the subphase is covered with a monolayer was obtained through the Young's law, $\cos\theta_1 = (\gamma_0/\gamma_1)\cos\theta_0$. Since all quantities in eq 9 are known except E, this variable can be determined for a given microsphere and η_s can be finally obtained (see Table I). Our η_s are relative close to measured η_s for other LE phases using the same procedure (for PDA, PPA, and DPPC, $0.2 \times 10^{-9} < \eta_s < 0.8 \times 10^{-9}$).[31] The uncertainties in the determination of the diffusion coefficients introduce uncertainties in E and, consequently, on the surface viscosities. For the objective pursued here of obtaining an estimation of the ζ parameter, this is not an important problem. Our results are presented in Table I. The ζ parameter is of the order of $1.6-3.8 \times 10^{-6}$ m.

To evaluate $q\zeta$, $q = 2\pi/l$ has to be estimated where l is a relevant repeat distance for domain growth. The relevant repeat distance has to be related to that distance where the description given by eq 4 is working. After a new domain is nucleated and starts to grow, there must be necessarily a nonstationary transient time, until domains reach a size from which domains grow in a stationary way. Domains are progressively growing and morphology is steadily evolving, when their size is in the range of $\sim 50-100$ μm ($q = 2\pi/l \sim 6.3 \times 10^4 - 13 \times 10^4$ μm^{-1}). From this size, they grow until reaching roughly $\sim 500-700$ μm for NA and EP monolayers (DODA ~ 100 μm), before colliding with other domains. Thus, $q\zeta$ is of the order of $0.1-0.5$. Therefore, according to eq 4, the growth of domains is dominated by viscous dissipation at the subphase, and viscous dissipation at the air−water interface plays a less important role, although it is not negligible. Since $q\zeta$ is not much less than 1, we cannot use directly the limiting equations given in ref 29, for viscous dissipation at subphase. An alternative solution will be given in the last section.

4.6. Movement of Tracer Microspheres around Growing Domains. The next experiments are addressed to study how particle tracers move around the growing domains. They could discriminate if around the growing domains there is a diffusion zone with a density profile or if LE is flowing in conjunction with a subphase flow. We dispersed in the LE phase hydrophobized silica microspheres as tracers and their movement was followed as a function of time. Nevertheless, first, it is necessary to test that dipolar interaction between silica microspheres and LC domains is low enough to be taken it into account. Otherwise, they would be bad tracers unless dipolar interaction is included. Difference in surface density gives rise LC domains to possess an excess dipole density with respect to the surrounding LE phase, pointing upward. Local electric fields around LC have been observed and measured with polystyrene spheres,[41] with ionizable groups on the surface exhibiting a dipolar moment pointing toward the water. In particular, the interaction is attractive over the whole range of separation distances, consistent with fact that dipoles in microspheres and in LC domains have opposite orientations. In silica microspheres, the dipolar moment must be very low because they have silanol (SiOH) surface groups and they were hydrophobized, as mentioned in the Experimental Section. To determine if this dipolar interaction is small enough, the movement of microspheres very close to domains in equilibrium (not growing) was tracked. In this situation, if there is some electrostatic interaction, particles that are in Brownian motion will move toward the LC domain at accelerated speeds as they get closer to the domain. We never observed anything like this. All particles wandered around domains, without an apparent interaction with domains. In Figure 9, we present examples of the movement of microspheres and of domains in equilibrium separated by a small distance for NA and EP monolayer, measured from a reference system placed at the Lab. As it is normal there are drifts along the LM, and what we observe in these experiments are a domain and microspheres traveling parallel to each other without any apparent interaction down to separations of the order of $7-8$ μm; we never observed any kind of drag in domains direction. Therefore, we consider the hydrophobized silica microspheres good tracers, and if there is some dipolar interaction, this is below our limit of detection.

In the next experiments, hydrophobized silica microspheres were dispersed in the LE phase, and their movement was followed close to the growing domains as a function of time with the aid of digitized pictures of the BAM VCR recordings (step = 1/25 s). We observed Brownian particles dragged onto the domains edge by virtue of a flow of material, where they were stuck along the domain edge. To observe the way those microspheres moved toward domains, we employed in addition to a coordinate frame attached to the Lab, where direct measurements were performed, two other coordinate frames, the monolayer frame and the moving boundary frame. In the

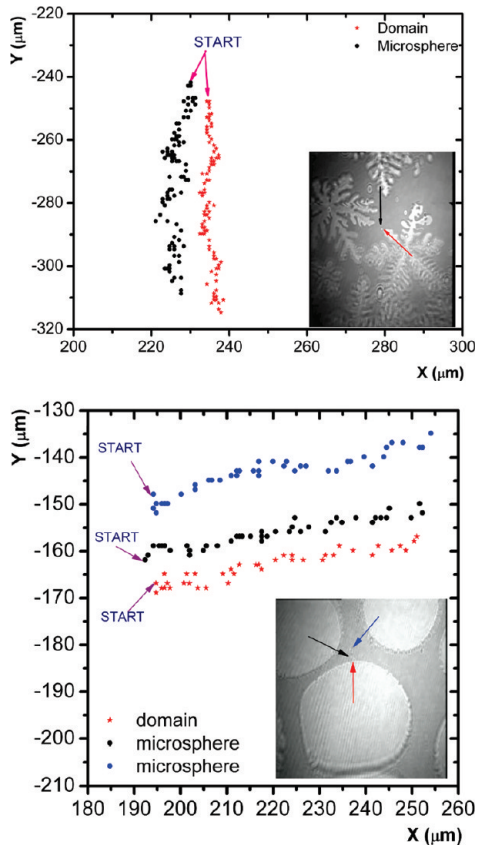

Figure 9. Position of microspheres immersed in LE phase as time elapsed wandering close to domains that are not growing (dots). Red stars correspond to a specific position in the domain edge, which is also moving due to drift in the monolayer. (Top) NA monolayer (T = 21.3 °C, Π = 4 mN/m), the particle was followed by 76 s, time step = 0.8 s. (Bottom) EP monolayer (T = 20.6 °C, Π = 10.6 mN/m), particles were followed by 5.04 s, time step 0.12 s.

first one, the frame is attached to a microsphere far from the growing domains. This is used to avoid macroscopic drift currents common in monolayers. The second frame is attached to the moving boundary of the domain under study; this is the frame used in theory (Section 2). The latter was selected using the following procedure. We observed with BAM microscopy how a domain and a particle were approaching to each other (in the Lab frame). We observed the exact position at the domain edge where the particle is trapped when they collide. Then, going backward in the BAM microscope VCR film, we were able to determine the sequence of positions as a function of time (each 1/25 s) on the domain edge that will give origin to the point where later the particle will be trapped (for short periods of time this can be done unambiguously). We used these positions on the domain edge to fix the origin of the moving boundary frame. As a consequence, positions of the microsphere and of the boundary points on the digitized BAM images allowed us to obtain particle positions with respect to the moving boundary frame, using elementary Galilean transformations. Examples of particle approach with respect to the moving boundary frame can be seen in Figures 10 and 11; in insets, we present the same information but from the monolayer frame. For all positions, we included the velocity component in the direction of the instantaneous origin of the moving boundary frame at the edge of the domain. Far from domains, microspheres are in Brownian motion, which is clearly superimposed on a drift toward domains (average speed ~25 μm/s for NA and ~23 μm/s for EP). When a microsphere is close to a domain, at a separation distance

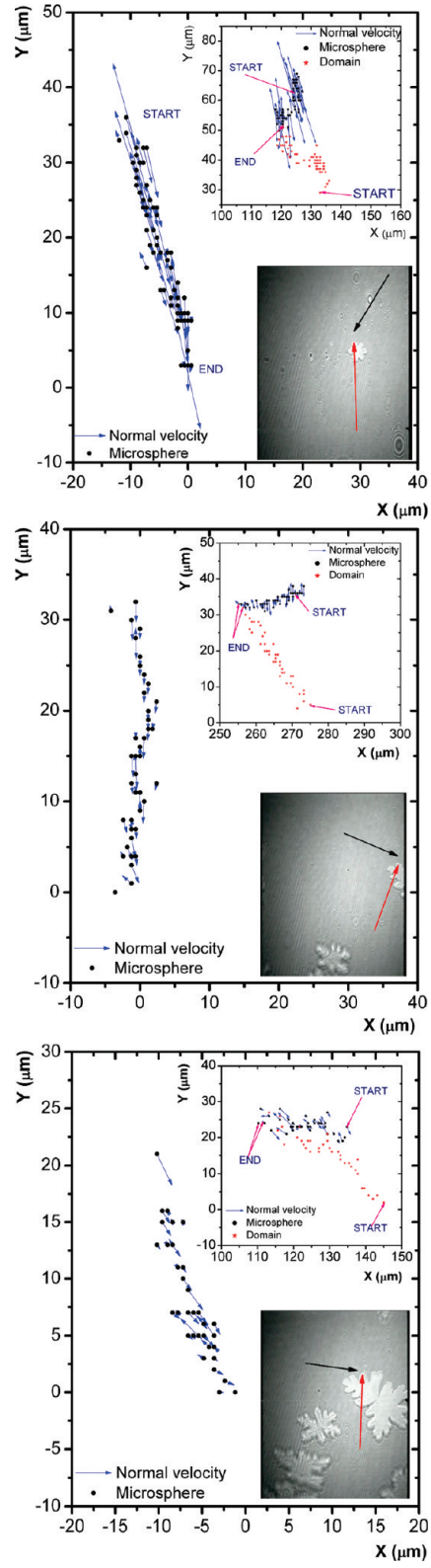

Figure 10. Tracer particle positions close to growing domains as time elapses (T = 21.0 °C, Π ~ 8.6 mN/m; upper panel, step 1/25 s; middle panel, step 2/25 s; lower panel, step 3/25 s) as observed from the LE/LC boundary frame defined on an EP domain during a continuous compression (compression rate ~6 cm^2/min). Particles collide with domains at the coordinate origin. Inset: Particle approach with respect to the monolayer frame defined by a microsphere far from the growing domains (microsphere positions are in black, domain edge positions that will give origin to the point where later the particle will be trapped are in red). Blue arrows indicate the velocity component in the direction of the instantaneous origin of the moving boundary frame (instantaneous radial velocity) at the edge of the domain.

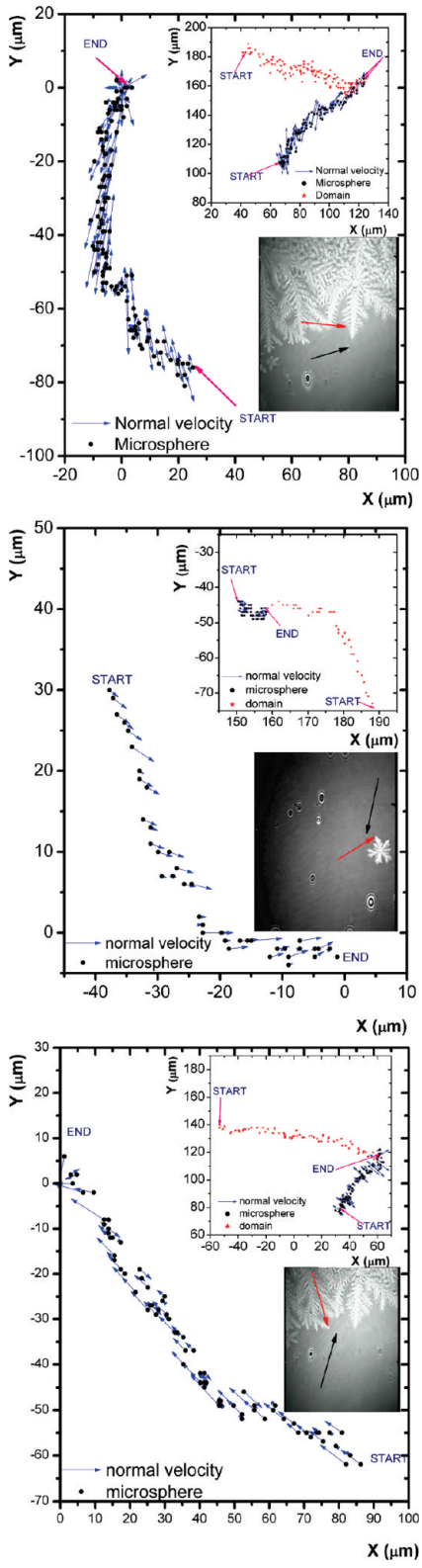

Figure 11. Tracer particle positions close to growing domains as time elapses (upper panel, step 3/25 s, $T = 23.1$ °C, $\Pi \sim 8.6$ mN/m; middle panel, step 2/25 s, $T = 23.3$ °C, $\Pi \sim 5.4$ mN/m; lower panel, step 3/25 s, $T = 23.1$ °C, $\Pi \sim 8.6$ mN/m) as observed from the LE/LC boundary frame defined on an NA domain during a continuous compression (compression rate ~5.5 cm^2/min). Inset: Particle approach with respect to the monolayer frame defined by a microsphere far from the growing domains (microsphere positions are in black, domain edge positions that will give origin to the point where later the particle will be trapped are in red). Blue arrows indicate the velocity component in the direction of the instantaneous origin of the moving boundary frame (instantaneous radial velocity) at the edge of the domain.

from a protruding part of a growing domain (finger or dendrite arm) in the range of 15 μm for EP and 29 μm for NA, usually a small change in the microsphere approach direction ensues. It seems as if the point that in the near future will trap the microsphere at the domain edge is dragging the microsphere onto it. This is visible as a change in particle approach direction in the monolayer frame, or in a change in direction of the velocity vectors in the moving boundary frame. However, the speed of the microspheres does not change when they are close to domains (average speed ~24 μm/s for NA and 22 μm/s for EP). On the average, the speed of the approaching particles is the same as when they are far from domains. An important observation is that when a particle and a domain tip are approaching, if they are not approaching in a head-on collision, microspheres laterally deviate from their course to reach the tip, revealing transverse flows to domain tips. This change is not related to dipolar interaction, as discussed at the beginning of this section.

The important drift shown by the tracer particles is hardly compatible with a diffusion zone due to a density profile around domains. In a small concentration profile, a Brownian particle of 2.47 μm probably will not notice it to modify its random walk motion in an important way. Particles should have to move slowly close to the domains $\sim(4Dt)^{1/2}$; no drift is expected. A small concentration profile practically will not affect the immersion of microspheres and consequently, a drag force change will be almost unnoticed to these Brownian particles. On the contrary, we have obtained evidence of Marangoni flow, that is, subphase flow driven by a difference in surface tension, related to the concentration gradient along the monolayer close to domains. The partially submerged microspheres are driven by the subphase convection flow (Marangoni) of the fluid where they are immersed in. The flow velocity of the subphase can be obtained by solving eq 3 in the stationary state, if appropriate boundary conditions are provided. Consider for simplicity, the case of a linear infinite LE/LC boundary along the Z-axis. Y-axis is along the downward normal to the air/water interface and the X-axis is normal to the LE/LC boundary away from the LE phase. Far from the growing boundary, the surface flow velocity $v_x(x,y,z)$ of the LE phase is a constant

$$v_x(x, y = 0, z) = -V \quad (x \gg 0) \tag{10}$$

Where $-V\boldsymbol{e}_x$ is the asymptotic surface flow velocity in the reference frame moving with the LE/LC boundary. The second boundary condition comes from the absence of flow in the LC phase. Consequently, from the coordinate frame moving with the LE/LC boundary

$$v_x(x, y = 0, z) = -V_s \quad (x < 0) \tag{11}$$

Where $V_s\boldsymbol{e}_x$ is the steady-state growth velocity of the LE/LC boundary (as seen from the monolayer). The third boundary condition is that flow in the direction normal to the LM is not allowed

$$v_y(x, y = 0, z) = 0 \tag{12}$$

It can be checked by direct substitution that the following expression is the solution to eq 3, in the moving frame that fulfills the boundary conditions[29]

$$\boldsymbol{v} = \left(-\frac{(U + 2V_s)}{2} - \frac{U}{\pi}\arctan\left(\frac{x}{y}\right) + \frac{Uxy}{\pi(x^2 + y^2)}\right)\boldsymbol{e}_x + \left(\frac{Uy^2}{\pi(x^2 + y^2)}\right)\boldsymbol{e}_y \quad (13)$$

Figure 12 shows $v_x(x,y,z)$ as a function of x as observed from the moving LE/LC boundary for different depths; $U = V - V_s$. To the right of the LE/LC boundary and for small depths, the flow velocity is approximately parallel to the surface and equal to $-V$. It gradually increases as one gets closer to the growing boundary. For $x < 0$ and small y, that is, below the LC phase, the magnitude of the flow velocity is close to V_s. Therefore, a partially submerged particle will present Brownian motion with a constant drift due to the flow under the LM. For a particle with its center at ~0.9 μm below the LM (as in our case), the drift of the particle will be constant up to 20 μm from the growing boundary. For closer distance, the particle will slightly decrease its velocity and will stop when it hits the LM, since our particle is protruding from the surface. All these events have been observed in our experiments. Notwithstanding, it is important to note that velocity field calculations are for the case of a linear infinite LE/LC boundary, and in the experiments there are irregular (tips) domain boundaries. However, approach velocities given by the model are close to the observed approach velocities measured in the experiments. Stability analysis of this problem have predicted transverse flows to domain tips as observed in our experiments.[29]

4.7. Morphology Evolution in Langmuir Monolayers. Apparently, we have lost the general picture given by the diffusional model proposing the existence of a diffusion zone, which with eq 7 and the boundary conditions given by eqs 1 and 2, successfully explains the pattern formation and the morphology evolution in LMs.[27,28] In the same way, apparently, we have also lost the connection with the morphology diagram with regions of different morphological structures,[6−11] determined by the control parameters Δ and ε, as explained above. Here, we will assess in what conditions the 2D hydrodynamic eq 4 can recover that picture related to pattern formation and to the morphology diagram. Equation 13 allows us to evaluate the last term of eq 4 through direct calculation

$$\partial_y \boldsymbol{v}(x, y = 0, z) = \frac{2(V - V_s)}{\pi}\boldsymbol{e}_x \quad (14)$$

Substituting this equation in eq 4 and applying the $\nabla_\perp \cdot$ operator on both sides of eq 4, we obtain the expression

$$\nabla^2\Pi = -\frac{2\eta(V - V_s)}{\pi}\frac{1}{x^2} \approx 0 \quad (15)$$

Here, $|d\gamma/d\rho_l|\nabla_\perp\rho_l = \nabla_\perp\Pi$ was used. The left side of this expression is negligible as revealed by dimensional analysis. Typical values for the dimensionless number $\eta(V - V_s)/\Pi \sim 10^{-6}$ m, except for distances of submicrometer order. Thus, eq 15 can be expressed as

$$\nabla_\perp\cdot\nabla_\perp\Pi = \nabla_\perp\cdot\left(\frac{d\Pi}{d\rho_l}\nabla_\perp\rho_l\right) = \frac{d\Pi}{d\rho_l}\nabla_\perp^2\rho_l + \nabla_\perp\rho_l\cdot\nabla_\perp\left(\frac{d\Pi}{d\rho_l}\right) = \left(\frac{d\Pi}{d\rho_l}\right)\nabla^2\rho_l + \left(\frac{d^2\Pi}{d\rho_l^2}\right)(\nabla\rho_l\cdot\nabla\rho_l) = 0 \quad (16)$$

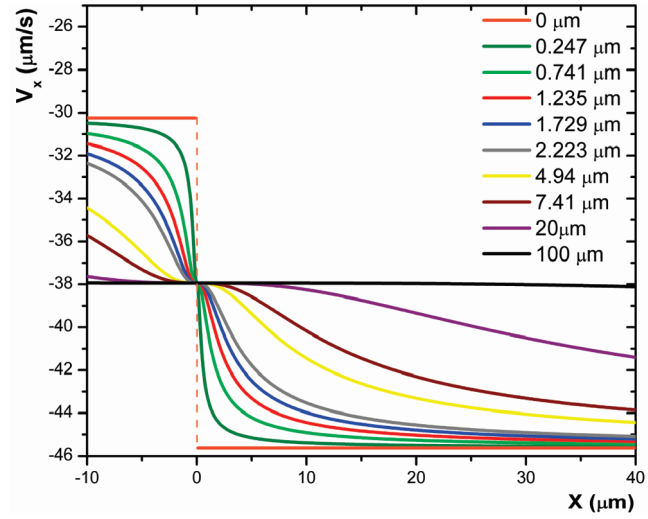

Figure 12. v_x as a function of position at different depths as given by eq 13.

To first order in the gradients, the last of the previous equations gives $\nabla^2\rho_l = 0$. Finally, from here eq 7 can be recovered, also to first order in the gradients. Therefore, eq 7 and the boundary conditions given by eqs 1 and 2 are still the basic equations followed by the system to form patterns. We recovered as the basic equation that governs the pattern formation, a Laplacian equation in the chemical potential.

Consider again, for simplicity, the case of a linear infinite LE/LC boundary along the Z-axis, where under steady state the interface is a straight line and the concentration profile $\rho_l(x)$ depends only on the x coordinate. In this condition, the tangential z-component of the flow vanishes, the surfactant current is strictly along the x direction, and $\boldsymbol{J}$ must be a constant, independent of x due to eq 5. Using eqs 5 and 6, we can write the following expression

$$v_x(x, y = 0, z)\frac{d\rho(x)}{dx} + \rho(x)\frac{dv_x(x, y = 0, z)}{dx} - D\frac{d^2\rho(x)}{dx^2} = 0 \quad (17)$$

Using eq 13 allows us to recast eq 17 in an equation similar to the steady-state diffusion equation in the Mullins-Sekerka theory[1]

$$\frac{d^2\rho(x)}{dx^2} + \frac{2}{l}\frac{d\rho(x)}{dx} = 0 \quad (18)$$

Where $l = (2D/V_s)[\rho_\infty/(\rho_s - \rho_o)]$ would be the diffusion length. This parameter can be estimated from our experimental data; the result is $l \sim 1$ μm. Amphiphile diffusion was estimated ($D \sim 10^{-11}$ m^2 s^{-1}) according to refs 42−44. Therefore, the diffusion length in our case is below our limit of resolution and is almost nonexistent.

5. Conclusion

In LMs, at low supersaturation, domains grow forming fractal structures without an apparent orientational order trough tip-splitting dynamics. Doublons are the building blocks producing domains with a fractal seaweed shape. When supersaturation is larger, there is a morphology transition from tip splitting to side branching. Here, structures grow with a pronounced orientational

order-forming dendrites, which are also fractal. Experimental evidence shows an important Marangoni flow during domain growth and in steady state, it is dominated by the bulk subphase viscous term, although the surface viscous term cannot be neglected. The equation that governs the pattern formation in LMs is a Laplacian equation in the chemical potential with the appropriate boundary conditions. However, the underlying physics involved in LMs is different from the underlying physics in the Mullins-Sekerka instability; diffusional processes are not involved. This is a new kind of instability that leads to pattern formation, where Marangoni flow is the key factor. The equations governing pattern formation in LMs are the same equations used by Müller-Krumbhaar and collaborators to analytically build a kinetic morphology phase diagram, where they include in the Gibbs−Thomson equation a supersaturation parameter and a capillary length with an anisotropy parameter. Therefore, an identical kinetic morphology diagram has to be followed in LMs. This diagram presents regions of different morphological structures and lines indicating transitions between them, discriminating between compact and fractal structures, as well as between dendrites and seaweeds. Our experiments agree with this diagram.

Acknowledgment. The support from SEP-CONACYT (81081) and DGAPA-UNAM (112508) is gratefully acknowledged. We also thank to C. Garza and S. Ramos for their technical support, to Alejandro Vazquez for his support in MATLAB, and to J. Fujioka for useful discussions.

References and Notes

(1) Langer, J. S. *Rev. Mod. Phys.* **1980**, *52*, 1.
(2) Ben-Jacob, E. *Contemp. Phys.* **1993**, *34*, 247.
(3) Glicksman, M. E.; Schaefer, R. J.; Ayers, J. D. *Metall. Trans. A* **1976**, *7*, 1747.
(4) Ben Amar, M.; Pomeau, Y. *Europhys. Lett.* **1986**, *2*, 307.
(5) Langer, J. S. *Science.* **1989**, *243*, 1150.
(6) Brener, E.; Müller-Krumbhaar, H.; Temkin, D. *Europhys. Lett.* **1992**, *17*, 535.
(7) Brener, E.; Kassner, K.; Müller-Krumbhaar, H.; Temkin, D. *Int. J. Mod. Phys. C* **1992**, *3*, 825.
(8) Brener, E.; Müller-Krumbhaar, H.; Temkin, D. *Phys. Rev. E.* **1996**, *54*, 2714.
(9) Brener, E.; Müller-Krumbhaar, H.; Temkin, D.; Abel, T. *Physica A* **1998**, *249*, 73.
(10) Ihle, T.; Müller-Krumbhaar, H. *Phys. Rev. Lett.* **1993**, *70*, 3083.
(11) Ihle, T.; Müller-Krumbhaar, H. *Phys. Rev. E* **1994**, *49*, 2972.
(12) Utter, B.; Ragnarsson, R.; Bodenschatz, E. *Phys. Rev. Lett.* **2001**, *20*, 4604.
(13) Stalder, I.; Bilgram, J. H. *Europhys. Lett.* **2001**, *56*, 829.
(14) Singer, H. M.; Bilgram, J. H. *Phys. Rev. E* **2004**, *70*, 31601.
(15) Miller, A.; Möhwald, H. *J. Chem. Phys.* **1987**, *86*, 4258.
(16) Akamatsu, S.; Bouloussa, O.; To, K.; Rondelez, F. *Phys. Rev. A* **1992**, *46*, 4505.
(17) Weidemann, G.; Vollhardt, D. *Langmuir* **1997**, *13*, 1623.
(18) Gehlert, U.; Vollhardt, D. *Langmuir* **1997**, *13*, 277.
(19) Iimura, K.; Yamauchi, Y.; Tsuchiya, Y.; Kato, T.; Suzuki, M. *Langmuir* **2001**, *17*, 4602.
(20) Flores, A.; Ize, P.; Ramos, S.; Castillo, R. *J. Chem. Phys.* **2003**, *119*, 5644.
(21) Karttunen, M.; Haataja, M. P.; Säily, M.; Vattulainen, I.; Holopainen, J. M. *Langmuir* **2009**, *25* (8), 4595.
(22) Nandi, N.; Vollhardt, D. *Chem. Rev.* **2003**, *103*, 4033.
(23) Weidemann, G.; Vollhardt, D. *Biophys. J.* **1996**, *70*, 2758.
(24) Vollhardt, D.; Emrich, G.; Gutberlet, T.; Fuhrhop, J.-H. *Langmuir* **1996**, *12*, 5659.
(25) Vollhardt, D.; Gutberlet, T.; Emrich, G.; Fuhrhop, J.-H. *Langmuir* **1995**, *11*, 2661.
(26) Hoffmann, F.; Stine, K. J.; Hühnerfuss, H. *J. Phys. Chem. B* **2005**, *109*, 240.
(27) Flores, A.; Corvere-Poiré, E.; Garza, C.; Castillo, R. *J. Phys Chem. B* **2006**, *110*, 4824.
(28) Flores, A.; Corvere-Poiré, E.; Garza, C.; Castillo, R. *Europhys. Lett.* **2006**, *74*, 799.
(29) Bruinsma, R.; Rondelez, F.; Levine, A. *Eur. Phys. J. E.* **2001**, *6*, 191.
(30) Edwards, D. A.; Brenner, H.; Wasan, D. T. *Interfacial Transport Processes and Rheology*; Butterworth-Heinemann: Boston, 1991.
(31) Sickert, M.; Rondelez, F.; Stone, H. A. *Europhys. Lett.* **2007**, *79*, 66005.
(32) Vollhardt, *J. Phys Chem C* **2007**, *111*, 6805.
(33) Albrecht, O.; Gruler, H.; Sackmann, E. *J. Phys. (Paris)* **1978**, *39*, 301.
(34) Krasteva, N.; Vollhardt, D.; Brezesinski, G.; Möhwald, H. *Langmuir* **2001**, *17*, 1209.
(35) Sickert, M.; Rondelez, F. *Phys. Rev. Lett.* **2003**, *90*, 126104.
(36) Fischer, Th. M. *Phys. Rev. Lett.* **2004**, *92*, 139603.
(37) Sickert, M.; Rondelez, F. *Phys. Rev. Lett.* **2004**, *92*, 139604.
(38) Forstner, M. B.; Käs, J.; Martin, D. *Langmuir* **2001**, *17*, 567.
(39) Selle, C.; Rücherl, F.; Martin, D. S.; Forstner, M. B.; Käs, J. A. *Phys. Chem. Chem. Phys.* **2004**, *6*, 5535.
(40) Fischer, Th. M.; Dhar, P.; Heinig, P. *J. Fluid Mech.* **2006**, *558*, 451.
(41) Nassoy, P.; Birch, W. R.; Andelman, D.; Rondelez, F. *Phys. Rev. Lett.* **1996**, *76*, 455.
(42) Caruso, F.; Grieser, F.; Murphy, A.; Thistlethwaite, P.; Urquart, R.; Almgren, M.; Wistus, E. *J. Am. Chem. Soc.* **1991**, *113*, 4838.
(43) Peters, R.; Beck, K. *Proc. Natl. Acad. Sci. U.S.A.* **1983**, *80*, 7183.
(44) Kim, S.; Yu, H. *J. Phys. Chem.* **1992**, *96*, 4034.

JP910344H